# scientific reports

OPEN

# Synthesis, molecular dynamics simulation and adsorption study of different pollutants on functionalized mesosilica

Rasool Pelalak[1,2], Roozbeh Soltani[3], Zahra Heidari[4], Rahime Eshaghi Malekshah[5], Mohammadreza Aallaei[6], Azam Marjani[7,8]✉, Mashallah Rezakazemi[9] & Saeed Shirazian[10]

Experimental and computational works were carried out on a new type of mesoporous silica. In the experimental section, functionalized hollow mesosilica spheres were prepared via a facile technique and then evaluated using some analytical techniques (FESEM, TEM, L-XRD, FTIR, BET-BJH, and TGA). The obtained results revealed that the synthesized material had hollow structure with a diamino-grafted porous shell. The molecular separation of crystal Violet (CV) and neutral Red (NR) dyes from water were investigated by adsorption process using the synthesized powder. Influence of adsorbent loading was evaluated as adsorption ability and dyes removal efficiency. Also, the obtained modeling results revealed appropriate fitting of data with non-linear Langmuir model. The theoretical studies were employed to study the adsorption and removal mechanism of cationic (CV and NR) and anionic (orange II (OII)) dyes using molecular dynamics calculations. Moreover, the simulation outcomes provided valuable information about quantum chemical properties including the HOMO–LUMO maps, chemical reactivity, global softness (σ) and hardness (η) for silica-linker-water-dyes components.

Reactive dyes and pigments are being extensively employed in industrial activites like textile, food, pharma, and have been recognized as a source of water pollutions[1–4]. In recent years, large amount of dyes are being released into the surface and groundwater causing harm to aquatic organisms, ecological systems and human health[4–7]. Among various synthetic dyes being used worlwide, crystal violet (CV), neutral red (NR), and orange II (OII) are cationic and anionic dyes, which are largely utillized in the industrial activities[8]. Toxic effects of dyes at specific amount and their mutagenesis, cancer-causing and carcinogenic effects has been reported widely[9–12]. The presence of dyes in the effleunt of wastewater treatment plants have been stated by several reports. Several treatment methods have been proposed and used for decontamination of wastewater including biological, sedimentation, adsorption, membrane, and filtration[13–17].

Adsorption as a highly efficient and costly separation/purification method has proved its ability for dye removal from aquatic solutions[18,19,20,21] and numerous adsorbents such as silica, zeolite, carbone based materials, ashes, and mineral clays have been extensively sythnesized and utillieezed in pollutants elimination from aqueous media[22,23]. One of the attractive classes of adsorbents is mesoporous silica (MPS) materials as inorganic polymers, which are superior candidates for many environmental processes due to their superior properties such as well-ordered pore systems and relatively inexpensive starting materials as well as high surface area[24–26]. A lot of attention has recently been focused on MPS for dye adsorption from wastewater[27–30]. Also, recent developments of the in vivo toxicity, bio-distribution and clearance of mesoporous materials in animal models have shown excellent long-term applications[31]. Surface modification or functionalizing of MPSs with some organic functional

[1]Institute of Research and Development, Duy Tan University, Da Nang 550000, Vietnam. [2]Faculty of Environmental and Chemical Engineering, Duy Tan University, Da Nang 550000, Vietnam. [3]Department of Chemistry, Arak Branch, Islamic Azad University, Arak, Iran. [4]Chemical Engineering Faculty, Sahand University of Technology, P.O. Box 51335-1996, Sahand New Town, Tabriz, Iran. [5]Department of Chemistry, College of Science, Semnan University, Semnan, Iran. [6]Department of Chemistry, Faculty of Science, Imam Hossein University, Tehran, Iran. [7]Department for Management of Science and Technology Development, Ton Duc Thang University, Ho Chi Minh City, Vietnam. [8]Faculty of Applied Sciences, Ton Duc Thang University, Ho Chi Minh City, Vietnam. [9]Faculty of Chemical and Materials Engineering, Shahrood University of Technology, Shahrood, Iran. [10]Laboratory of Computational Modeling of Drugs, South Ural State University, 76 Lenin Prospekt, Chelyabinsk, Russia 454080. ✉email: azam.marjani@tdtu.edu.vn

groups extremely improves the physical characteristics of MPSs like enhancing the available area and adsorption ability due to better interaction between the pollutant and adsorbent[26,28,32,33]. MPS functionalized with amino group with improved properties such as enhancement in surface area and also adsorption performance have been used as effective adsorbent for wastewater treatment approaches[15,26,34–36].

Beside the experimental works on development of MPSs, computational studies can be useful to understand the interaction at molecular level, and manipulate the functional groups for preparation of advanced porous materials for environmental applications. Molecular dynamics simulation is a great modelling tool which provides important understandings in molecular scale about adsorption process, interactions and transport properties[26,37]. Furthermore, usefule information about pollutant decomposition in atomic behavior can be provided by molecular dynamics computations.

In the current investigation, a molecular-level computational approach is utilized to understand the dye adsorption on the surface of MPS. Both experimental and computational works have been carried out. In the experiments, functionalization of MPS with amino group were investigated by one-pot synthesis method. Diamine-functionalized hollow mesosilica spheres (MPS-linker) adsorbent was fabricated and characterized with different tools, e.g. FESEM, XRD, FTIR, $N_2$ adsorption–desorption and TEM. Adsorption ability of MPS-linker adsorbent was evaluated in adsorption of CV and NR as cationic dyes and OII as anionic dye through comprehensive experimental and modeling investigations. In the modeling section, the molecular dynamic simulations were performed. The results of simulations provide very valuable information about gap energies, HOMO, LUMO, hardness, and reactivity of the interactions among dyes and MPS.

## Materials and methods

**Materials.** Diamino silane (1,4-Bis[3-(trimethoxysilyl)-propyl]ethylenediamine (DA) 97%) as coupling agent, tetraethyl orthosilicate (TEOS, ≥ 99.0%) as precursor and hexadecyltrimethylammonium bromide (CTAB) surfactant template were obtained from Sigma-Aldrich. Ultrapure ethanol and acetone were obtained from Merck, and purified water was used in all experiments.

**Synthesis procedure of adsorbent.** One-pot procedure proposed by Soltani et al. was used for synthesis of MPS-linker adsorbent, with some modifications[28,35,36]. In short, predetermined amount of CTAB and ammonia solution as a template, were added to purified water. The obtained solution was mixed at ambient temperature for 20 min. In the next step, a required amount of DA as functionalization material was added to the solution and sonicated for 5 min. Another 5 min sonication were applied to the mixture after adding 42.5 mL of TEOS, as silica source. The procedure was continued by magnetically stirring for 180 min. After that, the bottle was placed in the oven and kept for 12 h at 343 K. The obtained mixture was rinsed several times with deionized water, ethanol, and acetone then dried at 348 K overnight. The final product was refluxed overnight in order to eliminate CTAB (the reflux solution was ethanol/HCl 12 N 100:1). After cooling, the obtained mixture was sonicated for 5 min, then filtered and rinsed with ethanol and deionized water. At the end, the samples dried at 343 K for 24 h.

**Simulations.** The Materials Studio software was used for molecular quantum calculations through DMol3 module as reported in our previous work[26]. Prior to the computational calculations, the Hyperchem software was employed for initial optimizing the geometry of MPS-linker, water and dyes (CV, NR and OII). After that, the DMol3 module was employed for geometry and energy optimization, HOMO and LUMO energy levels, as well as COMSO sigma profile of the components. The simulated optimized structures were used for predicting the preferential adsorption of dyes on MPS-linker via adsorption locator and Forcite modules. A combination of MPS-linker/water/dye was selected for each run and the potential of their interactions were evaluated. In every simulation, a mixture of two molecules of dyes (NR or CV or OII), four molecules of water and one molecule of adsorbent were used to calculate the low energy configurations and energy distribution of the mixture.

## Results and discussion

**Characterization of adsorbent.** For characterizing surface functional groups of the produced adsorbent, the Fourier transform infrared spectroscopy (FTIR, Tensor 27, Bruker, Germany) with wavelength range of 400–4000 cm$^{-1}$ was applied using the KBr pellet technique. The obtained FTIR spectrum for the syntehsized adsorbent is presented in Fig. 1a. Also, the structure of MPS-linker is shown in Fig. 1a. The successful structure and composition of MPS-linker bearing diamino groups were observed by the obtained results[35,36,38,39]. The absorption bands around 461, 797, 1083 and 1197 cm$^{-1}$ are corresponded to bending mode, symmetric and asymmetric bending vibrations of the Si–O–Si[6]. The appearing band at 976 cm$^{-1}$ is assigned to stretching mode of Si–OH. Also, the band at 1457 cm$^{-1}$ is related to the C–H bending vibration mode. The recorded band at 1635 cm$^{-1}$ can be related to bending mode of –OH of the adsorbed $H_2O$ onto the surface[39]. The detected band around 2873–2923 cm$^{-1}$ can be attributed to the C–H stretching vibrations of the methylene groups in the DA structure[40]. The band located around 3255 cm$^{-1}$ is related to the –OH stretching vibration of adsorbed water and silanol groups[35]. The observed absorption band around 3407 cm$^{-1}$ can be associated to –NH and –NH$_2$– stretching vibration modes.

The crystalline structure of synthesized MPS-linker adsorbent was evaluated with the low-angle XRD (L-XRD) analyzer. The Siemens D5000 diffractometer XRD (Germany, scanning rate = 0.05° min$^{-1}$) was employed in 2θ = 0.8–10.0°. The obtained L-XRD result of MPS-linker is shown in Fig. 1b. As can be seen, the first peak observed at 2θ = 1.0–2.5° is a relatively sharp peak attributed to the semi-long-range ordered hexagonally arranged mesostructure of the silica[15,28]. Convenience in accessibility of adsorption sites can lead to overcome the mass transfer problems which overally improve the process efficiency[15,25,35,36].
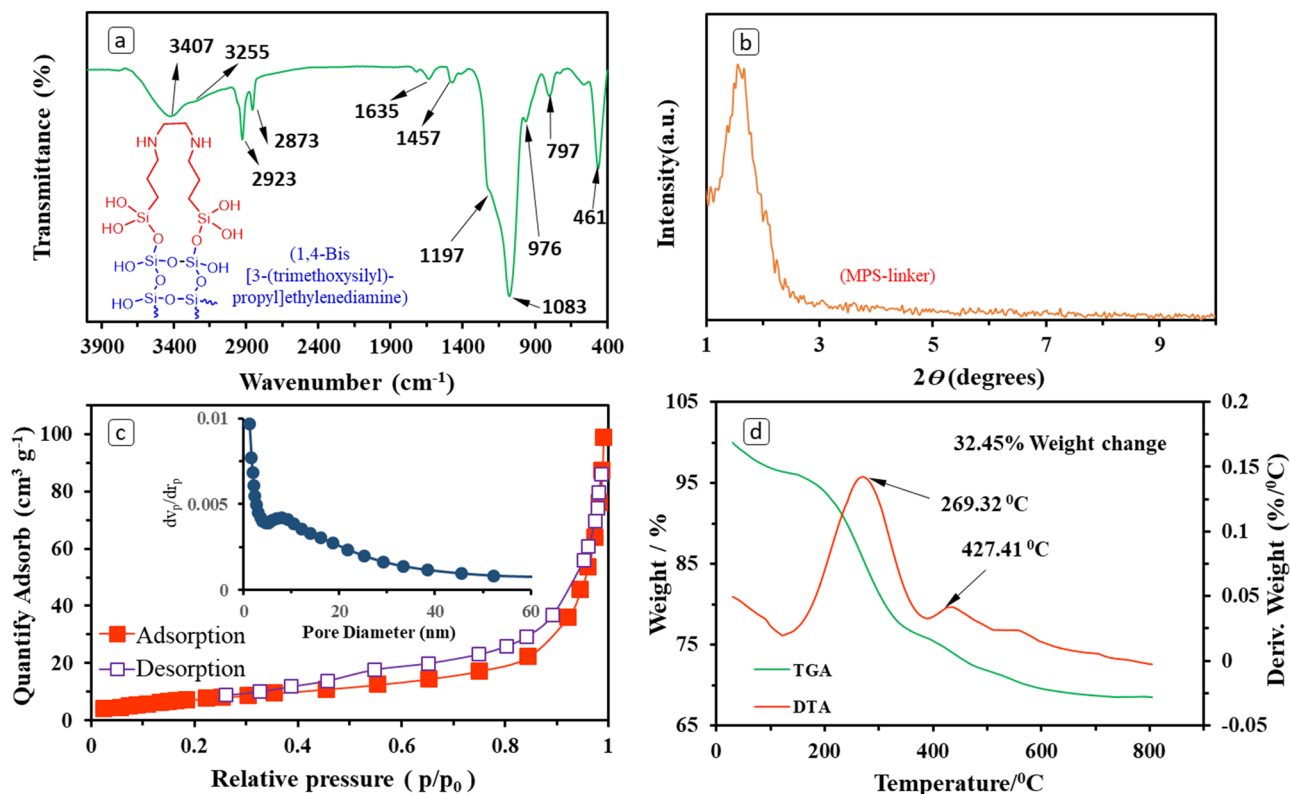
**Figure 1.** FTIR spectrum (**a**), L-XRD pattern (**b**), $N_2$ adsorption–desorption isotherms (**c**), and TGA/DTA results (**d**) for the synthesized adsorbent.

The surface properties were achieved by $N_2$ adsorption–desorption analysis, carried out at 77.3 K by using a Belsorp-mini II (Japan) and the obtained results are presented in Fig. 1c. As can be seen, the MPS-linker showed a combination of type IV(a) and V isotherms with a H3-hysteresis loop, according to the *IUPAC* assortment[27,41]. Also, the pore size distribution obtained by BJH model revealed that the size of pores can be lower and higher than 2 nm, indicating a bimodal micro-mesoporous structure for MPS-linker (the inset of Fig. 1c). The total pore volume ($V_{Tot}$) and specific surface area ($S_{BET}$) were around 0.15 $cm^3/g$ and 31 $m^2/g$, respectively. Also, the diameter of spheres, calculated by *Nahamin Pardazan Asia* software, were in the range of 1–4 μm.

Thermogravimetric analysis (TGA) was performed to assess the successful surface modification (Fig. 1d). This analysis was achieved under active argon flow in a thermal analyzer (SDT Q600, USA) in range between 30 and 800 °C and a heating rate of 20 °C $min^{-1}$. Figure 1d represents the thermal stability of prepared MPS-linker adsorbent. As can be inferred, a weight loss occurred below 200 °C was occured which can be due to the physisorbed water removal from the samples surface. The next weight reduction of MPS-linker adsorbent is observed above 300 °C which is primarily due to the destruction of the linker ($NH_2$-silane molecules) attached to the MPS-linker surface. TGA results indicated that about 32.45% weight loss was found for the as-prepared MPS-linker adsorbent and it can be said that the synthesized samples were stable up to 435 °C in an active argon flow atmosphere.

The field emission scanning electron microscope (FESEM) (Mira 3-XMU microscope) was utilized to investigate the surface morphology of synthesized adsorbent. The obtained FESEM micrographs are presented in Fig. 2a,b. The spherical morphology of the MPS-linker could be obviously observed. The hollow structure of the asprepared adsorbent can be inferred from cracked shells detected in the image which is depicted in Fig. 2b. In order to investigate the structural and morphorogical properties of the synthesized material, the transmission electron microscopy (TEM) was accomplished. The TEM images of the adsorbent structure are shown in Fig. 2c,d. As indicated, MPS-linker particles possess both ordered and interconnected wormhole pore structure. Parallel arrays of ordered mesochannels as well as wormhole channel motifs could be clearly seen in Fig. 2c,d. Wormhole pore structure can effectively improves the mass transfer and removes the diffusion barriers.

**Experimental results.** *Investigating the impact of MPS-linker dosage on adsorption process.* One of the significant factors on the adsorption efficiency is the amount of adsorbent loading. In this research, the effect of adsorbent dose on the removal efficiency of NR and CV was monitored, while the adsorbent dosages varied betweeen 0.25 and 1.0 g/L and other operating conditions were kept constant[35]. As can be seen in Fig. 3a,b the NR and CV removal were enhanced by increasing the MPS-linker dosage from 0.25 to 0.5 g/L, as expected[35]. The reason of this increment can be owing to the improvement in the availablilivy of adsorption sites of fabricated MPS-linker, by increasing the adsorbent loading. On the contrary, further increasing in the adsorbent
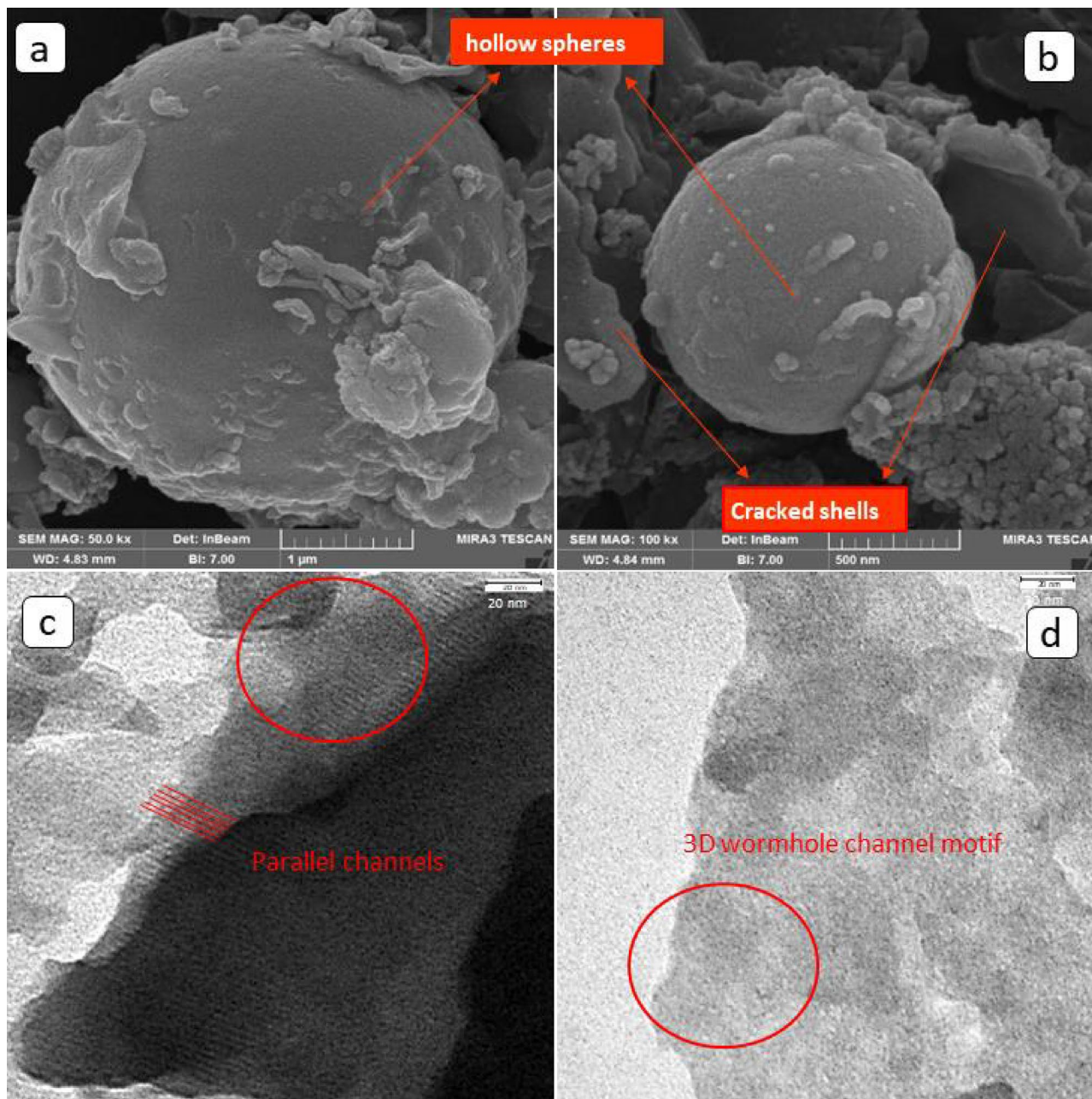
**Figure 2.** FESEM images (**a** and **b**), and TEM images (**c** and **d**) of the synthesized adsorbent.

loading (0.5–1 g/L) did not change the removal efficiency very significantly. Therefore, it can be revealed that the optimum dosage of MPS-linker is 0.5 g/L, and in all other tests were done at this value. In the case of adsorption capacity of MPS-linker, different trend was observed by increasing the adsorption dosage. As it can be seen in Fig. 3b, increasing the MPS-linker dosage reduced the adsorption capacity ($q_e$) in both CV and NR dyes. It can be said that by increasing the adsorbent in a constant initial concentration of CV and NR dyes as pollutant molecules, provided a low concentration gradient. This led to a negative influence on the pollutant attraction to the surface of MPS-linker.

*Isotherm studies.* The study of adsorption isotherms provide a deeper insight about adsorption capacity, adsorption mechanism between the pollutant and the adsorbent and the surface properties of MPS-linker. In this research, the behavior of CV and NR molecules adsorption on the prepared MPS-linker adsorbent were investigated using Langmuir and Freundlich isotherm models. According to Eqs. (1) and (2), the linear forms of Langmuir and Freundlich models can be achieved, respectively[35]:
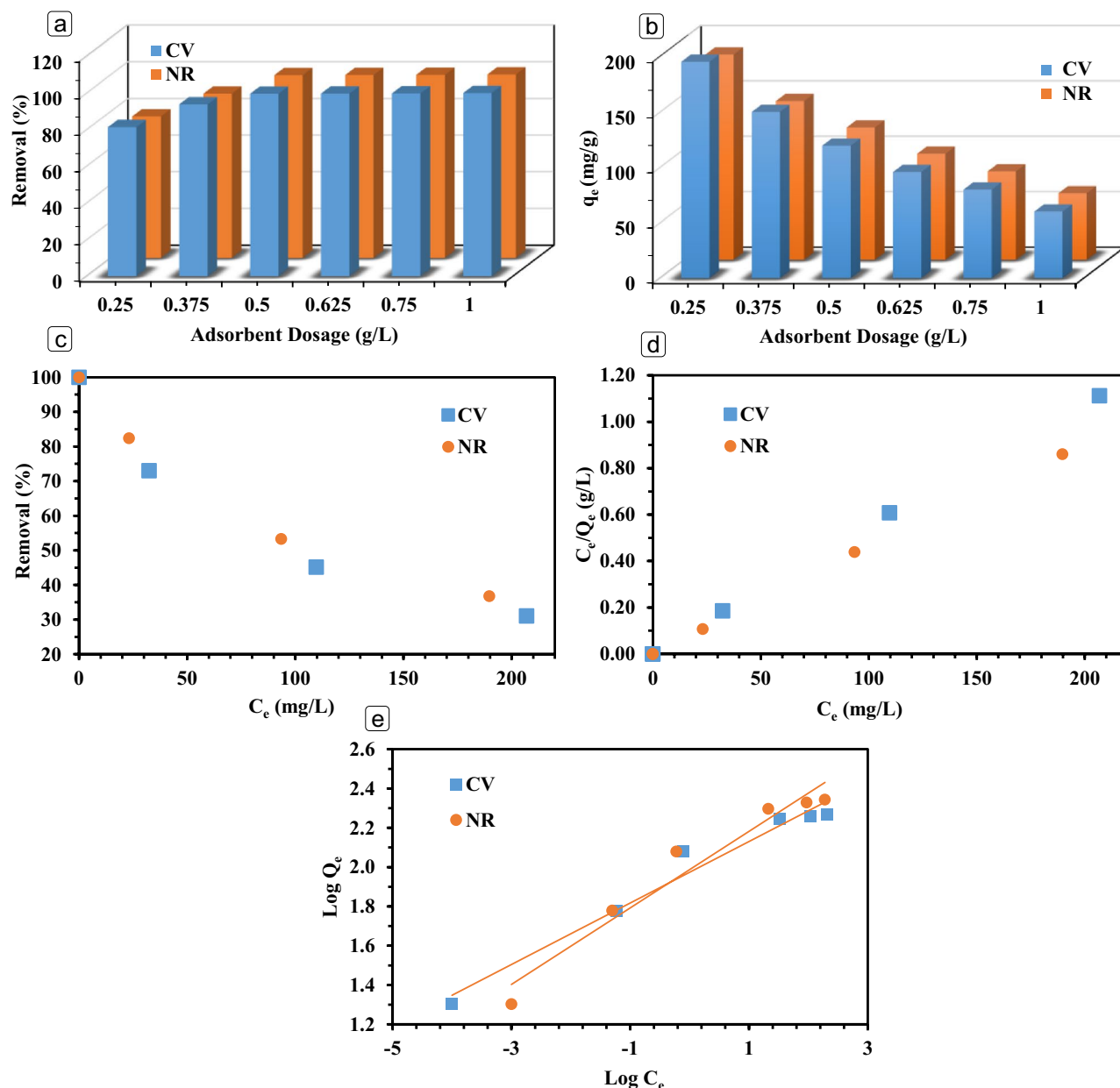
**Figure 3.** Impact of MPS-linker adsorbent loading on the CV and NR removal efficiency (**a**) and adsorption capacities (**b**), equilibrium isotherms (**c**), Langmuir (**d**) and Freundlich (**e**) models for CV and NR dyes adsorption on the synthesized MPS-linker adsorbent.

$$\frac{C_e}{q_e} = \frac{C_e}{q_{max}} + \frac{1}{q_{max} \, K_L} \tag{1}$$

$$\log q_e = \log K_f + \frac{1}{n} \log C_e \tag{2}$$

In these equations, $q_{max}$ is the maximum adsorption capacity (mg/g), $K_L$ is the constant value of the Langmuir model (L/mg). Also, $K_F$ and n present the constants in the Freundlich model. The results of adsorption isotherms for NR and CV adsorption on the synthesized MPS-linker adsorbent are shown in Fig. 3c–e. The adsorption isotherm parameter values are as follow: for CV: $K_L$ = 1.2, $K_F$ = 94.2 and n = 6.4; for NR: $K_L$ = 1.0, $K_F$ = 97.1 and n = 5.1. The linear regression coefficient ($R^2$) for Langmuir and Freundlich models were obtained as 0.999 and 0.960 for CV, and 0.999 and 0.938 for NR dyes, respectively. Therefore, it can be revealed that Langmuir isotherm model with higher $R^2$ more properly described the adsorption behavior of both NR and CV dyes[35].

A comparison of the adsorption capacity of NR and CV by the MPS-linker in this study with those stated in the literature is summarized in Table 1. It can be confirmed from the results that the synthesized MPS-linker adsorbent had almost the highest adsorption capacity for NR and CV dyes compared to other used adsorbents.

| Adsorbent | q_{max} for CV | q_{max} for NR | R² | References |
|---|---|---|---|---|
| MPS-linker | 185 | 222 | 0.999 | This work |
| Nanoporous carbon | 68.97 | – | 0.988 | [42] |
| Fe₃O₄/Chitosan/Glutaraldehyde nanocomposites | 105.467 | – | 0.996 | [43] |
| Modified kaolin nanoparticles | 96.10 | – | 0.992 | [44] |
| Gum arabic-cl-poly(acrylamide) nanohydrogel | 90.90 | – | 0.974 | [45] |
| Raw Tunisian Smectite Clay | 86.54 | – | 0.988 | [46] |
| Magnetic hollow spheres (Fe₂O₃) | – | 105 | 0.992 | [47] |
| Halloysite nanotubes | – | 54.85 | 0.999 | [48] |
| Typha orientalis carbon – MnCl₂ | – | 199.10 | 0.8714 | [49] |
| Typha orientalis carbon – Mn(NO₃)₂ | – | 198.37 | 0.9233 | [49] |
| Boron nitride nanoparticle | – | 26.20 | 0.995 | [50] |
| Peanut husk | – | 37.46 | 0.993 | [51] |

**Table 1.** Comparison of the capacity of adsorption for MPS-linker and other similar adsorbents (according to the Langmuir model).

This can be due to the presence of rich adsorption sites such as amine and hydroxyl groups, which can significantly provide a linkage between the MPS-linker surface and the NR and CV molecules[35].

**Modeling results.**  *Adsorption capacity analysis.*  The molecular dynamic simulations were investigated for adsorption of cationic dyes (CV and NR) on MPS-linker. Moreover, in this section the anionic dye adsorption ability of MPS-linker was studied for the orange II (OII) adsorption and the results were compared with the cationic dyes. In order to obtain the suitable position and energies of compounds, the structure of water, CV, NR, OII and MPS-linker were placed in the cell volume and optimized by Dmol3 module in Materials Studio software. The obtained results for the titled components as well as MPS-linker in the presence of water and dyes are shown in Fig. 4a–h. Based on the results, the total energy values of water, NR, CV, OII and MPS-linker were observed at $-75.91$, $-793.49$, $-1583.87$, $-1415.98$ and $-4653.41$ kcal/mol after optimization, respectively. In addition, the calculated values of adsorption energy were obtained about $-113.92$, $-247.00$ and $-166.01$ kcal/mol for MPS-linker-water-NR, MPS-linker-water-CV and MPS-linker-water-OII, respectively. The results of adsorption energy analysis indicated more negative adsorption energy value of compounds which represent trapping mechanism of dyes on the hollow mesosilica spheres. The adsorption energy of MPS-linker-water-NR was less negative than MPS-linker-water-CV and MPS-linker-water-OII. As a result, to remove NR dye using a chemical method, MPS-linker was less active in comparison with CV dye, meanwhile, to remove CV dye using a chemical method, MPS-linker was more active.

**Molecular calculations.**  In order to predict the distributions of surface polarity and molecular geometry of the compounds, Eckert et al.[52] established the analyses of quantum chemical through a statistical mechanics. Here, in order to characterize the probability distribution of charge density and the number of surface area fragments the Sigma ($\sigma$) profiles were obtained for all titled components. To obtain $\sigma$-profiles, quantum mechanical calculations were applied and the results are shown in Fig. 5. The $\sigma$-profile for the nonpolar bonding of water was located on $-0.0084$ e/Å² $<\sigma<+0.0084$ e/Å²[53]. The $\sigma$-surface appeared at $+0.015$ e/Å² can be related to the lone-pair electrons on oxygen elements in water. In addition, the peaks around $-0.015$ e/Å² were attributed to the polar hydrogen. The observed peaks in symmetric regions, denoted the durable hydrogen bond between water and other molecules[54]. The $\sigma$–profile of the non-H-bonding for NR dye demonstrated sharp peaks in range of $0-+0.015$ e/Å² which were related to the hydrogen elements in the methyl groups. Also, $\sigma$-profiles of the carbon of methyl groups, or the non–polar nitrogen groups of CV dye were detected between 0 and $+0.01$ e/Å²[55]. Furthermore, the obtained sigma profile of carbon atoms and the $\pi$-faced in the C rings were presented at about 0.0035 e/Å²[56]. In Fig. 5, the strong peak detected at about 0.008 e/Å² was related to the lone-pair electrons of oxygen in OII dye. In addition, very high intensity peak for the nitrogen in the OII structure was displayed about 0.0020 e/Å².

The observed peak of MPS-linker molecule around $+0.008$ e/Å² can be related to a pair of valence electrons on oxygen (Fig. 6). The presented peak at $-0.009$ e/Å² was attributed to the hydrogen atoms. Some low intensity peaks were detected around $+0.005$, which can be assigned to the electron-withdrawing fragments of the N groups in the MPS-linker structure. The high peaks between 0.010 and 0.018 e/Å² in MPS-linker-water-NR were associated to the cyclic nitrogen of adsorbed NR dye. Also, the obtained peaks of the sigma profile for MPS-linker-water-CV molecule observed in the region between $+0.010$ and $+0.021$ e/Å² were attributed to the N groups, and the presence of chlorine molecule. Finally, the observed peaks of the sigma profile for MPS-linker-water-OII molecule was detected around 0.0018 e/Å² which can be related to the nitrogen groups.

*Frontier molecular orbital analysis of compounds.*  The results of the highest occupied and the lowest unoccupied molecular orbitals (HOMOs and LUMOs, respectively) for differernt structures are presented in Fig. 7a–d. Some quantum chemical parameters can be obtained using the energy gap ($E_{gap}$) between frontier molecular orbitals (FMOs) such as electronegativity, electrophilicity index, the polarizability, global hardness and softness.
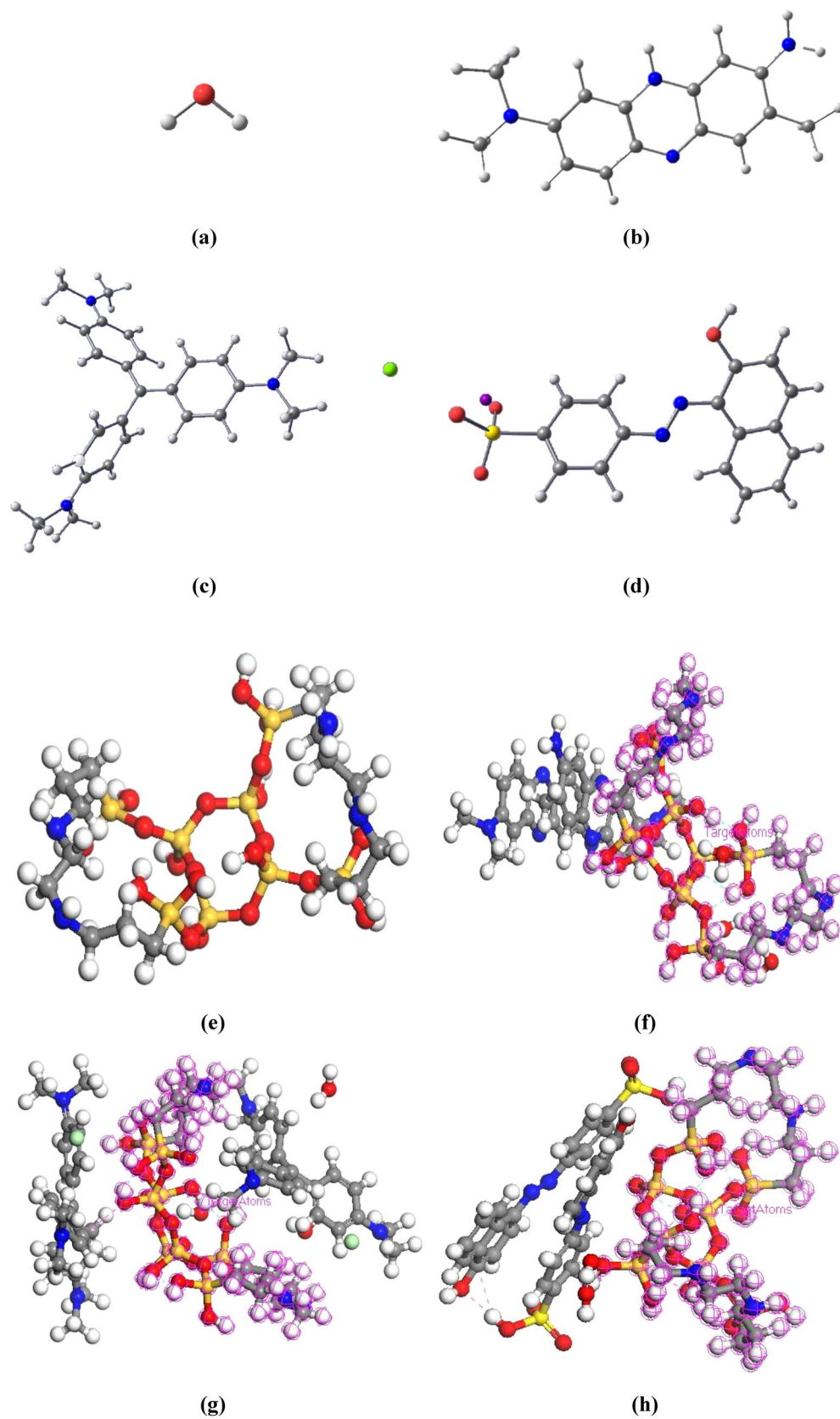
**Figure 4.** The optimized structures for water (**a**), NR (**b**), CV (**c**), OII (**d**), MPS-linker (**e**), MPS-linker-water-NR (**f**), MPS-linker-water-CV (**g**) and MPS-linker-water-OII (**h**).
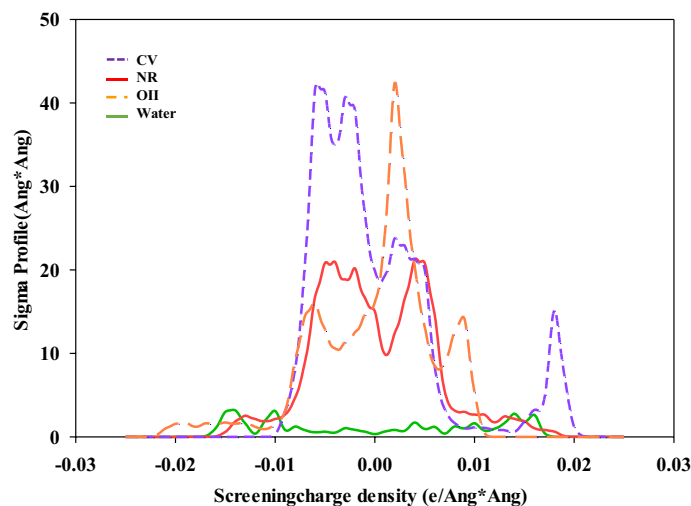
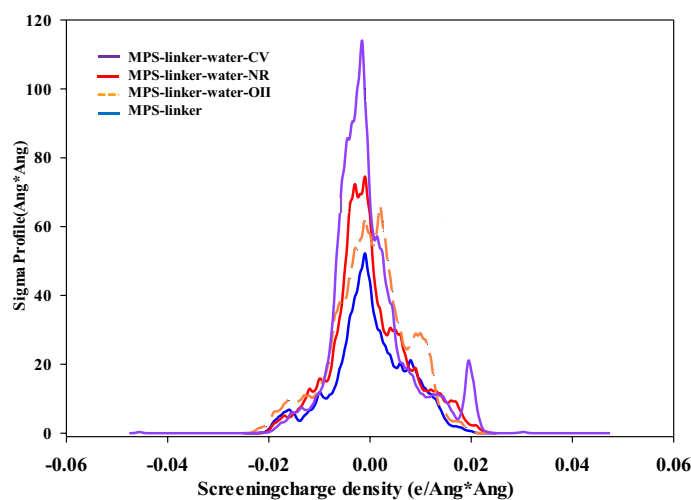**Figure 5.** The obtained Sigma profile for NR, CV, OII dyes and water molecules.



**Figure 6.** The obtained Sigma profile for MPS-linker-water-NR, MPS-linker-water-CV, MPS-linker-water-OII and MPS-linker.

The HOMO energy level of water, NR, CV and OII dyes were about $-0.2573, -0.1743, -0.1744$ and $-5.3570$ eV, respectively, meanwhile, the calculated LUMO energy level for water, NR, CV and OII dyes were positioned at about $+0.0567, -0.1073, -0.1215$ and $-3.7070$ eV, respectively. As shown in Fig. 7a–d, the HOMO energy levels of water were principally localized on the oxygen atom, whereas the LUMO energy levels were placed largely on hydrogen atom. Also, the HOMO and LUMOs levels of NR dye were mostly placed on the benzene ring (the N element) and on the hydrogen atom. In addition, in the electron charge distributions of HOMOs in CV dye were placed on the aromatic rings, nitrogen, and chlorine elements, whereas LUMO maps were distributed on the charge distribution of hydrogen atom. The HOMOs of OII dye were largely distributed on N atom as well as O atom of hydroxyl, while the LUMOs were generally localized on carbones of benzene ring and S element of dye.

The HOMO and LUMO maps of MPS-linker were measured at about $-10.1540$ and $+3.5270$ eV, respectively. The HOMOs were localized on N atoms of linker, while the LUMOs were mostly distributed on O and Si atoms of silica (Fig. 8a). Moreover, the energy values of $+7.4830$ and $-0.8720$ eV were reflected to HOMO and LUMO energy levels of MPS-linker-water-NR, respectively (Fig. 8b). The HOMOs of MPS-linker-water-NR were generally distributed on nitrogen elements of NR dye, while the LUMOs of this structure were mostly situated on rings linking to NR dye and linker of mesoporous silica. In addition, the HOMOs of MPS-linker-water-CV were distributed on chlorine, while, LUMOs were placed on rings of CV dye and Si element of mesoporous silica (Fig. 8c). The energy values of $-5.9070$ and $-3.0630$ eV in MPS-linker-water-CV were corresponded to the HOMOs and LUMOs, respectively. In addition, The HOMOs of MPS-linker-water-OII localized on N elements of OII dye, meanwhile, the LUMOs of this structure were distributed on S and O atoms of hydroxyl and carbones of benzene ring (Fig. 8d). The energy values of $-4.4980$ and $+4.0500$ eV in MPS-linker-water-OII were related to
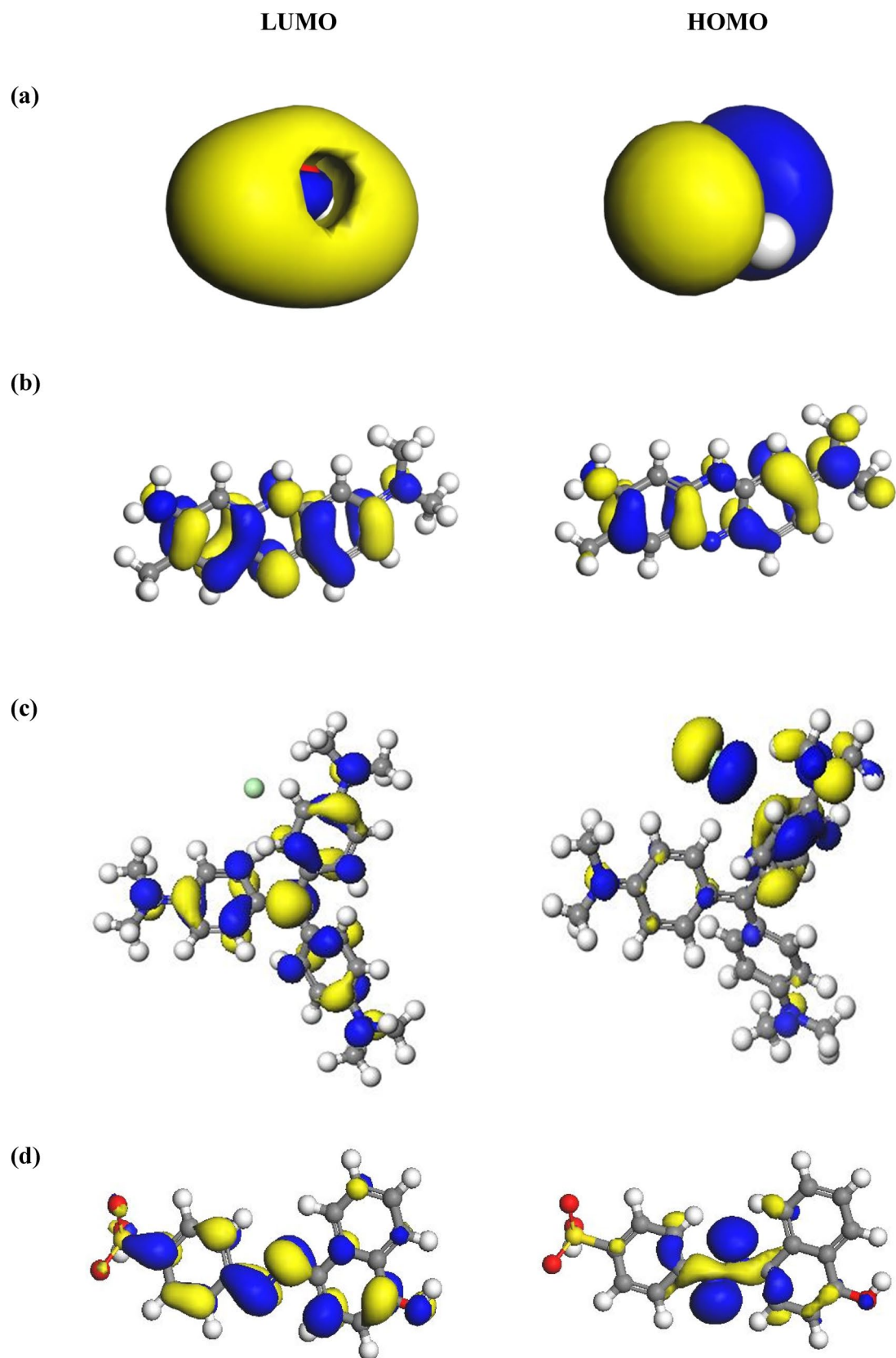
LUMO                    HOMO

**(a)**

**(b)**

**(c)**

**(d)**



**Figure 7.** The HOMO and LUMO energy levels for water (**a**), NR (**b**), CV (**c**) and OII (**d**) dye molecules.

LUMO                                    HOMO

**(a)**
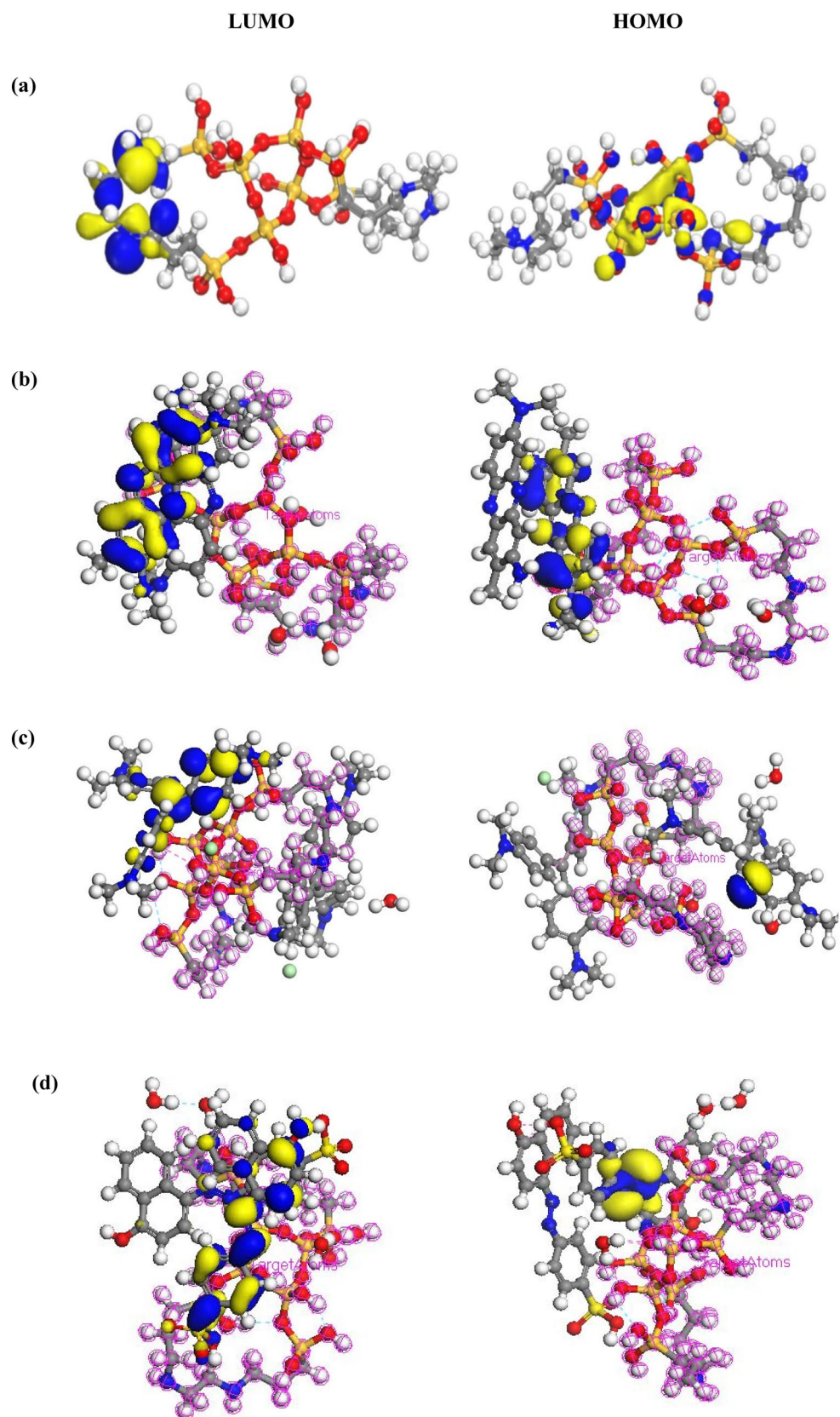
**(b)**

**(c)**

**(d)**

**Figure 8.** The HOMO and LUMO energy levels for MPS-linker (**a**), MPS-linker-water-NR (**b**), MPS-linker-water-CV (**c**) and MPS-linker-water-OII (**d**).

the HOMOs and LUMO energy levels, respectively. The corresponding energy gaps between HOMO and LUMO ($\Delta E = E_{LUMO} - E_{HOMO}$) for water, NR, CV, OII dyes, MPS-linker, MPS-linker-water-NR, MPS-linker -water-CV and MPS-linker-water-OII molecules were about 0.3140, 0.0670, 0.0529, 1.6500, 13.681, 1.2400, 0.4300 and 0.4480 eV, respectively. Due to the lower HOMO–LUMO energy gap value of CV dye compared to NR molecules, it can be concluded that the CV adsorbtion on the MPS-linker is occurred easier due to high reactivity of CV molecule.

*Chemical hardness ($\eta$) and softness ($\sigma$) of compounds.* The chemical reactivity is of great importance for determination of the structure reactivity. Based on the chemical reactivity, molecules can be divided into hardness ($\eta$) and softness ($\sigma$) molecules and the hard structures are less reactive compared to the soft ones. The chemical hardness is a significant physicochemical property for understanding the behavior of chemical material. The soft/hard molecules have small/large energy gap. By increasing the $E_{gap}$ value, the chemical reactivity of component is decreased while the stability is increased. The values of $\eta$ and $\sigma$ can be obtained using Eqs. (3) and (4)[54,26].

$$\eta = \left( \frac{I - A}{2} \right) \tag{3}$$

$$\sigma = \frac{1}{\eta} \tag{4}$$

In Eq. (3), $I$ refers to the the ionization potential (-$E_{HOMO}$). Also, $A$ denotes the electron affinity (−$E_{LUMO}$). According to above mentioned Eqs., the smaller value of hardness means more reactivity and vice versa[57,58]. The chemical hardness of NR, CV, OII, MPS-linker-water-NR, MPS-linker-water-CV, and MPS-linker-water-OII structures were about 0.0349, 0.0235, 0.8250, 0.6200, 0.2150, and 0.3080 eV, respectively. According to the results, the hardness of MPS-linker-water-CV was less than MPS-linker-water-NR, and MPS-linker-water-OII. As a result, MPS-linker-water-CV is the more soft and less stable. The chemical hardness of MPS-linker-water-NR, MPS-linker-water-CV, and MPS-linker-water-OII were about 1.2400, 0.4300 and 0.4480 eV, respectively. Therefore, it can be concluded that the chemical reactivity of MPS-linker-water-CV was more than NR and OII in the presence of MPS-linker.

## Conclusions

In this research the MPS-linker adsorbent was successfully prepared via a facile one-pot sol–gel-hydrothermal method. Different characterization analyses such as FESEM, TEM, FTIR, L-XRD, BET/BJH and TGA were utilized to investigate the physicochemical properties of fabricated adsorbent. The adsorption performance of produced MPS-linker was studied in removal of natural red and crystal violet dyes. The influence of initial adsorbent amount was evaluated on removal efficiency and adsorbtion capacities. The results obtained after linear fitting of the Langmuir and Freundlich model indicated that the Langmuir model provides a better fit to the experimental data. The molecular dynamics simulations were investigated for adsorption of both cationic (NR and CV) and anionic (OII) dyes and the results were compared. The optimization of structures were carried out by the Dmol3 module. The outcomes demonstrated the adsorption ability of functionalized silica for both anionic and cathionic dyes in water environment. The chemical reactivity, global hardness and softness were measured from frontier molecular orbitals. Due to less HOMO–LUMO, $E_{gap}$ of CV dye on MPS-linker adsorbent, the chemical reactivity and softness of CV dye were higher compared to other dyes. The results predicted the great potential of MPS-linker adsorbent for the CV removal compared to NR and OII dyes.

## References

1. Lellis, B., Fávaro-Polonio, C. Z., Pamphile, J. A. & Polonio, J. C. Effects of textile dyes on health and the environment and bioremediation potential of living organisms. *Biotechnol. Res. Innov.* **3**, 275–290. https://doi.org/10.1016/j.biori.2019.09.001 (2019).
2. El-Ahmady El-Naggar, N., Rabei, N. H. & El-Malkey, S. E. Eco-friendly approach for biosorption of Pb²⁺ and carcinogenic Congo red dye from binary solution onto sustainable Ulva lactuca biomass. *Sci. Rep.* **10**, 16021. https://doi.org/10.1038/s41598-020-73031-1 (2020).
3. Katheresan, V., Kansedo, J. & Lau, S. Y. Efficiency of various recent wastewater dye removal methods: a review. *J. Environ. Chem. Eng.* **6**, 4676–4697. https://doi.org/10.1016/j.jece.2018.06.060 (2018).
4. Pelalak, R., Alizadeh, R., Ghareshabani, E. & Heidari, Z. Degradation of sulfonamide antibiotics using ozone-based advanced oxidation process: experimental, modeling, transformation mechanism and DFT study. *Science of The Total Environment* (2020).
5. Gunture, *et al.* Soluble graphene nanosheets for the sunlight-induced photodegradation of the mixture of dyes and its environmental assessment. *Sci. Rep.* **9**, 2522. https://doi.org/10.1038/s41598-019-38717-1 (2019).
6. Heidari, Z. *et al.* Degradation of furosemide using photocatalytic ozonation in the presence of ZnO/ICLT nanocomposite particles: experimental, modeling, optimization and mechanism evaluation. *J. Mol. Liq.* **319**, 114193 (2020).
7. Sharma, S. & Bhattacharya, A. Drinking water contamination and treatment techniques. *Appl. Water Sci.* **7**, 1043–1067. https://doi.org/10.1007/s13201-016-0455-7 (2017).
8. Madrakian, E., Ghaemi, E. & Ahmadi, M. Magnetic solid phase extraction and removal of five cationic dyes from aqueous solution using magnetite nanoparticle loaded platanusorientalis waste leaves. *Anal. Bioanal. Chem. Res.* **3**, 279–286. https://doi.org/10.22036/abcr.2016.39075 (2016).
9. Kamble, G. S. & Ling, Y.-C. Solvothermal synthesis of facet-dependent BiVO4 photocatalyst with enhanced visible-light-driven photocatalytic degradation of organic pollutant: assessment of toxicity by zebrafish embryo. *Sci. Rep.* **10**, 12993. https://doi.org/10.1038/s41598-020-69706-4 (2020).

10. Mani, S. & Bharagava, R. Exposure to crystal violet, its toxic, genotoxic and carcinogenic effects on environment and its degradation and detoxification for environmental safety. *Rev. Environ. Contam. Toxicol.* **237**, 71–104. https://doi.org/10.1007/978-3-319-23573-8_4 (2015).

11. Kastury, F., Juhasz, A., Beckmann, S. & Manefield, M. Ecotoxicity of neutral red (dye) and its environmental applications. *Ecotoxicol. Environ. Saf.* **122**, 186–192. https://doi.org/10.1016/j.ecoenv.2015.07.028 (2015).

12. Chung, K.-T. Azo dyes and human health: a review. *J. Environ. Sci. Health Part C* **34**, 233–261. https://doi.org/10.1080/10590501.2016.1236602 (2016).

13. Soltani, R., Marjani, A., Moguei, M. R. S., Rostamia, B. & Shirazian, S. Novel diamino-functionalized fibrous silica submicro-spheres with a bimodal-micro-mesoporous network: Ultrasonic-assisted fabrication, characterization, and their application for superior uptake of Congo red. *J. Mol. Liq.* **294**, 111617 (2019).

14. Pelalak, R., Heidari, Z., Soltani, H. & Shirazian, S. Mathematical model for numerical simulation of organic compound recovery using membrane separation. *Chem. Eng. Technol.* **41**, 345–352 (2018).

15. Soltani, R., Marjani, A., Hosseini, M. & Shirazian, S. Meso-architectured siliceous hollow quasi-capsule. *J. Colloid Interface Sci.* **570**, 390–401 (2020).

16. Bayomie, O. S. *et al.* Novel approach for effective removal of methylene blue dye from water using fava bean peel waste. *Sci. Rep.* **10**, 7824. https://doi.org/10.1038/s41598-020-64727-5 (2020).

17. Soltani, H., Pelalak, R., Heidari, Z., Ghadiri, M. & Shirazian, S. CFD simulation of transport phenomena in wastewater treatment via vacuum membrane distillation. *J. Porous Med.* **19**, 515–526 (2016).

18. Ouachtak, H. *et al.* Experimental and molecular dynamics simulation study on the adsorption of Rhodamine B dye on magnetic montmorillonite composite $\gamma$-Fe$_2$O$_3$@Mt. *J. Mol. Liq.* **309**, 113142 (2020).

19. Oyelude, E. O., Awudza, J. A. M. & Twumasi, S. K. Equilibrium, kinetic and thermodynamic study of removal of eosin yellow from aqueous solution using teak leaf litter powder. *Sci. Rep.* **7**, 12198. https://doi.org/10.1038/s41598-017-12424-1 (2017).

20. Zabihi, S. *et al.* In situ polymerized FDU-12/PMMA and FDU-12/polyamide 6 nanocomposites for Cd(II) adsorption. *Chem. Eng. Technol.* https://doi.org/10.1002/ceat.202000298 (2020).

21. Soltani, R., Marjani, A. & Shirazian, S. A hierarchical LDH/MOF nanocomposite: single, simultaneous and consecutive adsorption of a reactive dye and Cr(vi). *Dalton Trans.* **49**(16), 5323–5335 (2020).

22. Rehman, F., Volpe, P. L. O. & Airoldi, C. Free amino and imino-bridged centres attached to organic chains bonded to structurally ordered silica for dye removal from aqueous solution. *J. Environ. Manag.* **133**, 135–143. https://doi.org/10.1016/j.jenvman.2013.11.042 (2014).

23. Heidari, Z., Alizadeh, R., Ebadi, A., Oturan, N. & Oturan, M. Efficient photocatalytic degradation of furosemide by a novel sono-precipted ZnO over ion exchanged clinoptilolite nanorods. *Sep. Purif. Technol.* **242**, 116800 (2020).

24. Bremmell, K. E. & Prestige, C. A. Enhancing oral bioavailability of poorly soluble drugs with mesoporous silica based systems: opportunities and challenges. *Drug Dev. Ind. Pharm.* **45**, 349–358 (2019).

25. Huang, C.-H., Chang, K.-P., Ou, H.-D., Chiang, Y.-C. & Wang, C.-F. Adsorption of cationic dyes onto mesoporous silica. *Micropor. Mesopor. Mater.* **141**, 102–109 (2011).

26. Pelalak, R. et al. Molecular dynamics simulation of novel diamino-functionalized hollow mesosilica spheres for adsorption of dyes from synthetic wastewater. *J. Mol. Liq.* **322**, 114812 (2021).

27. Marjani, A., Soltani, R., Pishnamazi, M., Rezakazemi, M. & Shirazian, S. Functionalized pollen-like mesoporous silica for Cr (VI) removal. *Micropor. Mesopor. Mater.* **310**, 110531 (2020).

28. Soltani, R., Marjani, A. & Shirazian, S. Facile one-pot synthesis of thiol-functionalized mesoporous silica submicrospheres for Tl (I) adsorption: isotherm, kinetic and thermodynamic studies. *J. Hazard. Mater.* **371**, 146–155 (2019).

29. Cestari, A. R. *et al.* The removal of reactive dyes from aqueous solutions using chemically modified mesoporous silica in the presence of anionic surfactant—the temperature dependence and a thermodynamic multivariate analysis. *J. Hazard. Mater.* **161**, 307–316 (2009).

30. Soltani, R. *et al.* Preparation of COOH-KCC-1/polyamide 6 composite by in situ ring-opening polymerization: synthesis, characterization, and Cd(II) adsorption study. *J. Environ. Chem. Eng.*, 104683 (2020).

31. Lu, J., Liong, M., Li, Z., Zink, J. I. & Tamanoi, F. Biocompatibility, biodistribution, and drug-delivery efficiency of mesoporous silica nanoparticles for cancer therapy in animals. *Small* **6**, 1794–1805 (2010).

32. Fu, X., Chen, X., Wang, J. & Liu, J. Fabrication of carboxylic functionalized superparamagnetic mesoporous silica microspheres and their application for removal basic dye pollutants from water. *Micropor. Mesopor. Mater.* **139**, 8–15 (2011).

33. Anbia, M. & Salehi, S. Removal of acid dyes from aqueous media by adsorption onto amino-functionalized nanoporous silica SBA-3. *Dyes Pigm.* **94**, 1–9 (2012).

34. Hartono, S. B. *et al.* Improving adsorbent properties of cage-like ordered amine functionalized mesoporous silica with very large pores for bioadsorption. *Langmuir* **25**, 6413–6424 (2009).

35. Roozbeh, S., Marjani, A., Hosseini, M. & Shirazian, S. Mesostructured hollow siliceous spheres for adsorption of dyes. *Chem. Eng. Technol.* **43**, 392–402 (2019).

36. Soltani, R., Marjani, A. & Shirazian, S. Shell-in-shell monodispersed triamine-functionalized SiO2 hollow microspheres with micro-mesostructured shells for highly efficient removal of heavy metals from aqueous solutions. *J. Environ. Chem. Eng.* **7**, 102832 (2019).

37. Du, H. & Miller, J. D. A molecular dynamics simulation study of water structure and adsorption states at talc surfaces. *Int. J. Miner. Process* **84**, 172–184 (2007).

38. Zarei, F., Marjani, A. & Soltani, R. Novel and green nanocomposite-based adsorbents from functionalised mesoporous KCC-1 and chitosan-oleic acid for adsorption of Pb (II). *Eur. Polym. J.* **119**, 400–409 (2019).

39. Pelalak, R. & Heidari, Z. Lithographically cut multiwalled carbon nanotubes: opening caps, controlling length distribution, and functionalization. *J. Dispersion Sci. Technol.* **35**, 808–814 (2014).

40. Pelalak, R., Alizadeh, R. & Ghareshabani, E. Enhanced heterogeneous catalytic ozonation of pharmaceutical pollutants using a novel nanostructure of iron-based mineral prepared via plasma technology: a comparative study. *J. Hazard. Mater.* **392**, 122269 (2020).

41. Soltani, R., Marjani, A., Soltani, R. & Shirazian, S. Hierarchical multi-shell hollow micro–meso–macroporous silica for cr (Vi) adsorption. *Sci. Rep.* **10**, 1–12 (2020).

42. Güzel, F., Sayğılı, H., Sayğılı, G. A. & Koyuncu, F. Decolorisation of aqueous crystal violet solution by a new nanoporous carbon: equilibrium and kinetic approach. *J. Ind. Eng. Chem.* **20**, 3375–3386. https://doi.org/10.1016/j.jiec.2013.12.023 (2014).

43. Azari, A. *et al.* Experimental design, modeling and mechanism of cationic dyes biosorption on to magnetic chitosan-lutaraldehyde composite. *Int. J. Biol. Macromol.* **131**, 633–645. https://doi.org/10.1016/j.ijbiomac.2019.03.058 (2019).

44. Sun, P. *et al.* Mechanistic links between magnetic nanoparticles and recovery potential and enhanced capacity for crystal violet of nanoparticles-coated kaolin. *J. Clean. Prod.* **164**, 695–702. https://doi.org/10.1016/j.jclepro.2017.07.004 (2017).

45. Sharma, G. *et al.* Fabrication and characterization of Gum arabic-cl-poly(acrylamide) nanohydrogel for effective adsorption of crystal violet dye. *Carbohydr. Polym.* **202**, 444–453. https://doi.org/10.1016/j.carbpol.2018.09.004 (2018).

46. Hamza, W., Dammak, N., Hadjltaief, H. B., Eloussaief, M. & Benzina, M. Sono-assisted adsorption of cristal Violet dye onto Tunisian Smectite clay: characterization, kinetics and adsorption isotherms. *Ecotoxicol. Environ. Saf.* **163**, 365–371. https://doi.org/10.1016/j.ecoenv.2018.07.021 (2018).

47. Iram, M., Guo, C., Guan, Y., Ishfaq, A. & Liu, H. Adsorption and magnetic removal of neutral red dye from aqueous solution using $Fe_3O_4$ hollow nanospheres. *J. Hazard. Mater.* **181**, 1039–1050. https://doi.org/10.1016/j.jhazmat.2010.05.119 (2010).
48. Luo, P. *et al.* Study on the adsorption of neutral Red from aqueous solution onto halloysite nanotubes. *Water Res.* **44**, 1489–1497. https://doi.org/10.1016/j.watres.2009.10.042 (2010).
49. Zhang, J. *et al.* Adsorption of neutral Red onto Mn-impregnated activated carbons prepared from Typha orientalis. *Biores. Technol.* **99**, 8974–8980. https://doi.org/10.1016/j.biortech.2008.05.018 (2008).
50. Zheng, T. *et al.* Functional group driven adsorption of neutral red by boron nitride nanoparticles: experimental and theoretical studies. *Mater. Res. Exp.* **6**, 0950a0951. https://doi.org/10.1088/2053-1591/ab33a6 (2019).
51. Han, R., Han, P., Cai, Z., Zhao, Z. & Tang, M. Kinetics and isotherms of neutral Red adsorption on peanut husk. *J. Environ. Sci.* **20**, 1035–1041. https://doi.org/10.1016/S1001-0742(08)62146-4 (2008).
52. Eckert, F. & Klamt, A. Fast solvent screening via quantum chemistry: COSMO-RS approach. *ALCHE J.* **49**, 369–385 (2004).
53. Suganthi, S. *et al.* Structural analysis and investigation of molecular properties of Cefpodoxime acid, a third generation antibiotic. *J. Mol. Struct.* **1108**, 1–15 (2016).
54. Rahbar, M., Morsali, A., Bozorgmehr, M. R. & Beyramabadi, S. A. Quantum chemical studies of chitosan nanoparticles as effective drug delivery systems for 5-fluorouracil anticancer drug. *J. Mol. Liq.* **302**, 112495 (2020).
55. Lemaoui, T. *et al.* Prediction of electrical conductivity of deep eutectic solvents using COSMO-RS sigma profiles as molecular descriptors: a quantitative structure-property relationship study. *Ind. Eng. Chem. Res.* **59**, 13343–13354 (2020).
56. Rezakazemi, M., Albadarin, A., Walker, G. & Shirazian, S. Quantum chemical calculations and molecular modeling for methylene blue removal from water by a lignin-chitosan blend. *Int. J. Biol. Macromol.* **120**, 2065–2075 (2018).
57. Mishra, V. R., Ghanavatkar, C. W., Mali, S. N., Chaudhari, H. K. & Sekar, N. Schiff base clubbed benzothiazole: synthesis, potent antimicrobial and MCF-7 anticancer activity, DNA cleavage and computational study. *J. Biomol. Struct. Dyn.* **38**, 1772–1785 (2020).
58. Venkateshan, M. & Suresh, J. Synthesis, physicochemical and quantum chemical studies on a new organic NLO crystal: cinnamoyl-proline. *J. Mol. Struct.* **1180**, 826–838 (2019).

## Acknowledgements

## Author contributions

R.P.: Writing-draft, Simulations; R.S.: Experiments, Analysis, Characterizations; Z.H.: Validation, Software; R.E.M.: Conceptualization, Modeling; M.A.: Writing-review, Computations, Software; A.M.: Supervision, Funding, Validation; M.R.: Writing-review, validation, software; S.S.: Supervision, Funding.

## Competing interests

The authors declare no competing interests.

## Additional information

**Correspondence** and requests for materials should be addressed to A.M.

**Reprints and permissions information** is available at www.nature.com/reprints.

**Publisher's note** Springer Nature remains neutral with regard to jurisdictional claims in published maps and institutional affiliations.